

# Validation of electron temperature gradient turbulence in the Columbia Linear Machine

X. R. Fu,<sup>1</sup> W. Horton,<sup>1</sup> Y. Xiao,<sup>2</sup> Z. Lin,<sup>2</sup> A. K. Sen,<sup>3</sup> and V. Sokolov<sup>3</sup>

<sup>1</sup>University of Texas at Austin, Austin, Texas 78712, USA

<sup>2</sup>University of California, Irvine, California 92697, USA

<sup>3</sup>Plasma Research Laboratory, Columbia University, New York, New York 10027, USA

(Received 4 November 2011; accepted 24 January 2012; published online 6 March 2012)

The electron temperature gradient (ETG) mode, which is a universal mechanism for turbulent electron thermal transport in plasmas, is produced and verified in steady-state, collisionless hydrogen plasma of the Columbia Linear Machine. Electron temperature profiles with strong gradients are produced by DC acceleration in a remote biased mesh and subsequent thermalization. Finite amplitude  $\sim 5\%$ , steady-state oscillations at  $\sim 0.3 - 0.5$  MHz (in the plasma frame), with azimuthal wave numbers  $m \sim 14 - 16$  and parallel wave number  $k_{\parallel} \sim 0.01 \text{ cm}^{-1}$  are measured. The massively parallel gyrokinetic toroidal code is used to study these modes. The results show that in the linear phase, the dispersion relation is consistent with kinetic theory. In the nonlinear stage, very strong nonlinear wave coupling gives rise to an inverse cascade of the energy from the fastest growing high- $m$  modes to low- $m$  nonlinear oscillations, which are consistent with the measured azimuthal mode spectrum. The radial structure of the fluctuation also agrees with the experiment. An inward radial shift of the peak of the potential fluctuation occurs during the nonlinear saturation and fluctuation fingers extend radially out to the edge plasma. Three-wave coupling mechanism is involved in the saturation of ETG modes. The simulations show a power law spectrum of the turbulence which suggests that the renormalization theory is appropriate to interpret the turbulent thermal flux. © 2012 American Institute of Physics. [doi:10.1063/1.3686148]

## I. INTRODUCTION

The standard model for a universal turbulent electron transport across various magnetic confinement geometries is the electron temperature gradient (ETG) form of drift wave turbulence. The driving mechanism is the electron temperature gradient and the physical mechanism is readily understood from the Carnot cycle made up from the  $\mathbf{E} \times \mathbf{B}$  convection of the plasma in drift wave vortices. The ETG instability involves convection of the thermal electron distribution and does not require a magnetically trapped electron distribution. The electron temperature gradient is expressed by  $dT_e/dr = -T_e/L_{Te}$  where  $L_{Te}$  is defined as the local electron temperature gradient scale length. The instability is robust with a fast growth rate of the order of a few tenths of  $v_{te}/L_{Te}$  (when  $k_{\perp}\lambda_{De} \ll 1$ ), where  $v_{te}$  is the electron thermal velocity. The resulting turbulence has now been used to explain electron transport in many tokamak confinement systems including NSTX (Refs. 1 and 2), Tore-Supra,<sup>3</sup> and TCV (Ref. 4). However, the fluctuations in these experiments were not directly measured. Recently, Mazzucato *et al.*<sup>5</sup> use reflectometry in NSTX to measure part of the  $k$ -spectrum for ETG.

Basic steady-state university-scale hydrogen plasma experiments on the Columbia Linear Machine (CLM) have been carried out that directly measure the fluctuations with specially designed low capacitance probes that allow the measurement of plasma potentials up to MHz frequencies. The conditions for the ETG instability are created with a new plasma source that has a two-part acceleration/heating mesh with a higher and variable voltage on the inner disk mesh  $r < r_1$  and lower voltage on the outer ring mesh

$r_1 < r < a$ . This arrangement allows the formation of electron temperature profiles with a continuous range of temperature gradient scale lengths  $L_{Te}$ . The plasma density profile can be maintained as flat in CLM which simplifies the theory of the ETG instability. Using high speed data acquisition equipment, Wei *et al.*<sup>6</sup> obtain steady-state fluctuation data and have reported that the spectrum is consistent with the ETG instability.<sup>6</sup> In Table I, we summarize the parameters of the CLM hydrogen plasma used in these experiments.

As we will show the fluctuations in the rest frame of the plasma are in the range of 100–500 kHz and the wavenumbers are high ranging up to  $k_y\rho_e \sim 0.5$  for the fastest growing modes in the case of sharp electron temperature gradients. However, the probe data show that fluctuations with much longer wavelength dominate the spectrum, thus there is clearly a need for nonlinear simulations of the system to understand the experimental data.

In Sec. II, we will briefly summarize the major results from the CLM experiments. In Sec. III, we will report the linear theory of ETG for the CLM. The dominant oscillations in the experiments have much longer wave length than the fastest growing linear mode, which suggests a strong nonlinear coupling. In Sec. IV, computer simulations with the gyrokinetic toroidal code (GTC) are analyzed. These simulations show the same feature of an inverse cascade of fluctuation energy from large wavenumber modes to the small wavenumber modes. The thermal fluxes calculated from the GTC code are compared with a nonlinear theory.<sup>7</sup> We also scan over the temperature gradient scale length and compare with experimental results. In Sec. V, we give the conclusions.

TABLE I. Machine and plasma parameters for a typical ETG experiment in the Columbia Linear Machine.

Machine length	$L = 150$ cm
Minor radius	$a = 3.3$ cm
Electron temperature (on axis)	$T_{e0} = 16.5$ eV
Ion temperature	$T_i = 3.1$ eV
Electron density	$n_e = 3.2 \times 10^9$ cm $^{-3}$
Magnetic field	$B = 1000$ G
Electron temperature scale length ( $r = 1.8$ cm)	$L_{Te} = 0.33$ cm
Parallel wave number	$k_z = 0.003$ cm $^{-1}$
Electron gyro-frequency	$\omega_{ce} = 1.76 \times 10^{10}$ rad/s
Plasma frequency	$\omega_{pe} = 3.09 \times 10^9$ rad/s
Electron thermal velocity (on axis)	$v_{te0} = 1.70 \times 10^8$ cm/s
Ion sound speed	$c_s = 3.97 \times 10^6$ cm/s
Electron gyro-radius (on axis)	$\rho_{e0} = 0.0097$ cm
Ion gyro-radius	$\rho_i = 0.18$ cm
Debye length (on axis)	$\lambda_{De0} = 0.055$ cm

## II. ETG MODES IN THE CLM EXPERIMENTS

CLM is a basic plasma experiment in a cylindrical linear machine that is capable of producing steady-state collisionless hydrogen plasmas confined by an external magnetic field. The plasma is produced by a DC discharge in the source region. For electron heating, a tungsten mesh is biased in the transition region with a suitably positive potential to accelerate the plasma electrons. These electrons then thermalize on the neutrals to create a higher temperature in the center ( $\sim 15$  eV) relative to the edge ( $< 1$  eV) and create a sharp electron temperature gradient. The resulting low density hydrogen plasma ( $\sim 10^9/\text{cm}^3$ ) flows into the experiment (central) cell which is about 1.5 m long and 3 cm in radius and immersed in a 0.1 T homogeneous magnetic field. Ion temperature remains low ( $\sim 2$  eV). The relevant parameters are listed in Table I and the radial profiles of plasma density  $n_e(r)$ , electron temperature  $T_e(r)$ , and ion temperature  $T_i(r)$  obtained are shown in Fig. 1(a). The density profile is almost flat in the region of turbulence.

Specially designed high-resolution twin Langmuir probes are placed inside the plasma to measure the electric potential. The power spectrum of signals from the twin probes is shown in Fig. 1(b). When the electron temperature gradient is above a threshold ( $L_{Te} < 0.428$  cm), strong signals are found around 2.2 MHz. After subtracting the  $\mathbf{E} \times \mathbf{B}$  rotational frequency due to the bias potential, the frequency of the mode in the plasma rest frame is about 0.3 MHz. The radial profiles of potential fluctuation are measured and show that the maximum fluctuation is located close to the point of the sharpest electron temperature gradient (smallest  $L_{Te}$ ), as in Fig. 2. Detailed analysis of the signals shows that three azimuthal modes  $m = 14, 15,$  and  $16$  are dominant in the steady-state fluctuation signal.<sup>6</sup>

## III. LINEAR PROPERTIES OF ETG IN A CYLINDER

In this section, we will report the linear properties of ETG modes for the CLM plasma. The linear properties of ETG have been studied thoroughly and the dispersion rela-

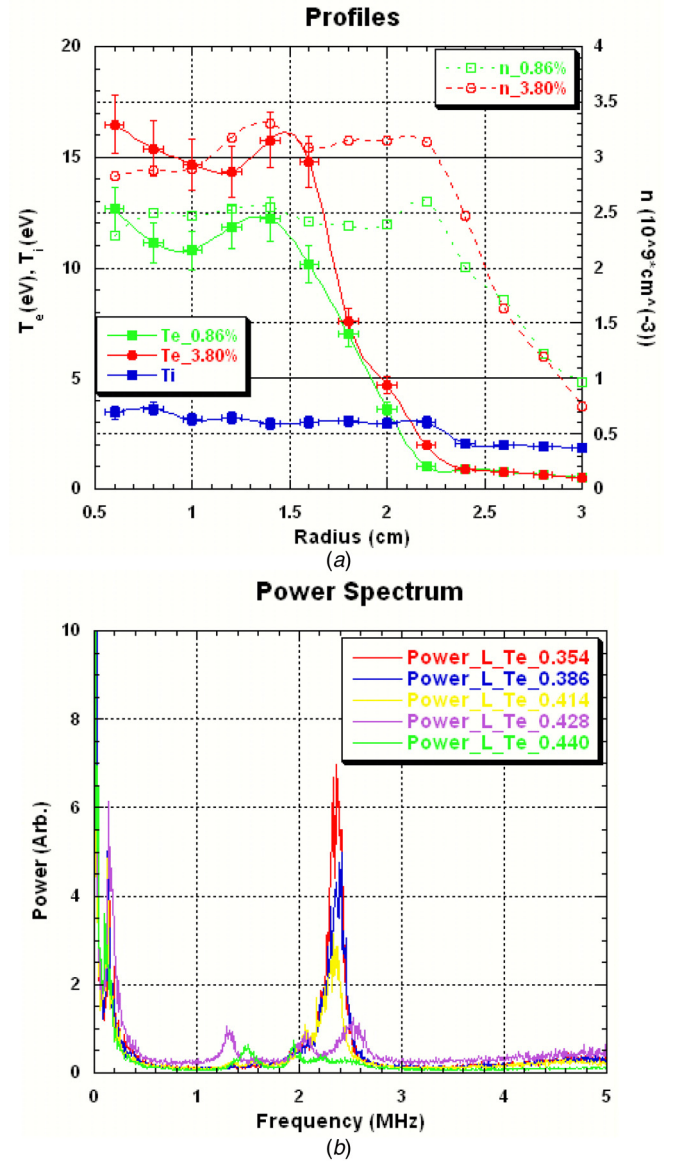


FIG. 1. (Color online) (a) Radial profiles of electron temperature  $T_e$ , ion temperature  $T_i$ , and plasma density  $n_e$  measured in the CLM. Two sets of data with two different bias voltages (thus different temperature gradient) are shown. A strong electron temperature gradient is produced between  $r = 1.5$  cm and  $r = 2.2$  cm. Note that the density in the region of  $1.5 \text{ cm} < r < 2.2$  cm is nearly flat. The electron velocity distribution is close to a local Maxwell-Boltzmann distribution with the temperature  $T_e(r)$  and a constant electron density  $n_e$ . The ion temperature is also constant and less than  $1/5$  the electron temperature. (b) The power spectra of the signals picked up by the high frequency probe are recorded for various temperature gradients ( $a/L_{Te}$ ). For strong enough temperature gradient  $L_{Te} < 0.428$  cm, signals are found to be peaking around 2.4 MHz in the laboratory frame. Reprinted with permission from Ref. 6. Copyright 2010 American Institute of Physics.

tion of slab ETG mode in the fluid limit with no density gradient is given by:<sup>8</sup>

$$\begin{aligned}
 & \left[ \frac{T_e}{T_i} + (k_{\perp} \lambda_{De})^2 + \frac{k_{\perp}^2 \rho_e^2}{2} \right] \left( \frac{\omega}{\omega_{ce}} \right)^3 + \frac{k_{\perp}^2 \rho_e^2}{2} k_y \rho_e \frac{\rho_e}{L_{Te}} \left( \frac{\omega}{\omega_{ce}} \right)^2 \\
 & + \left( \frac{k_{\perp}^2 \rho_e^2}{4} - \frac{1}{2} \right) (k_{\parallel} \rho_e)^2 \left( \frac{\omega}{\omega_{ce}} \right) \\
 & + \frac{1}{4} \left( 1 + \frac{k_{\perp}^2 \rho_e^2}{2} \right) k_y \rho_e \frac{\rho_e}{L_{Te}} (k_{\parallel} \rho_e)^2 = 0.
 \end{aligned} \quad (1)$$

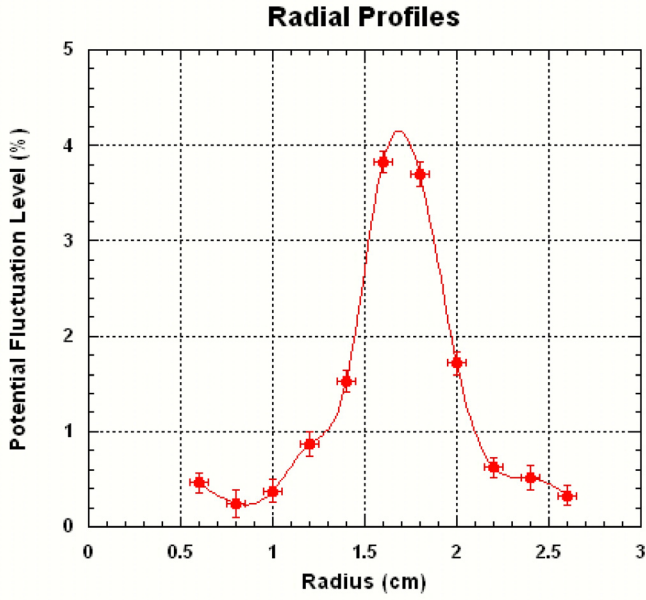


FIG. 2. (Color online) The radial profile of the electric potential fluctuation measured in the CLM, peaking around  $r = 1.7$  cm. Reprinted with permission from Ref. 6. Copyright 2010 American Institute of Physics.

This slab model is equivalent to the toroidal ETG mode (e.g., Ref. 7) in the limit of large toroidal curvature  $R/L_{Te}$  and large safety factor  $q = rB_t/RB_p$ . We use these relationships in the reduction of the toroidal GTC simulation code to the cylindrical CLM plasma.

We solve the cubic dispersion relation in Eq. (1) for eigenmodes for CLM parameters and plot the dispersion relation in Fig. 3. Three modes (roots) exist and the unstable Mode 2 is the source of turbulence. The remaining modes are damped and may absorb wave energy received by the nonlinear transfer from the unstable mode. In the plasma rest frame, the frequency of the most unstable mode is  $\omega \approx 2\pi \times 1.5$  MHz with wave number  $k_y \rho_e \approx 0.3$  or the poloidal wave number  $m \approx 70$ . In the laboratory frame, the plasma is rotating so the corresponding laboratory frequency is  $\omega_{\text{lab}} = m\Omega + \omega(\mathbf{k})$ , where  $\Omega \equiv E_r/(rB) \sim 2\pi \times 130$  kHz for nearly rigid-body rotation.

#### IV. GYROKINETIC SIMULATIONS WITH GTC CODE

GTC (Ref. 9) is a sophisticated massively parallel gyrokinetic particle simulation code, which has been successful in simulating toroidal ion temperature gradient (ITG) mode, collisionless trapped electron mode (CTEM), toroidal ETG, Alfvén eigenmodes, and other plasma phenomena.<sup>10–13</sup> We adapt the toroidal GTC code to study the cylindrical plasmas by taking the limit of infinite constant  $q$  and setting the equivalent major radius  $R_0 \gtrsim 1/k_{\parallel}$ . In this section, we will first focus on results for the set of parameters listed in Table I and later do a parametric scan of the  $T_e$  gradient and parallel wave number  $k_{\parallel}$ .

##### A. Numerical results

Based on the parameters in Table I, the space-time units in the code are normalized as

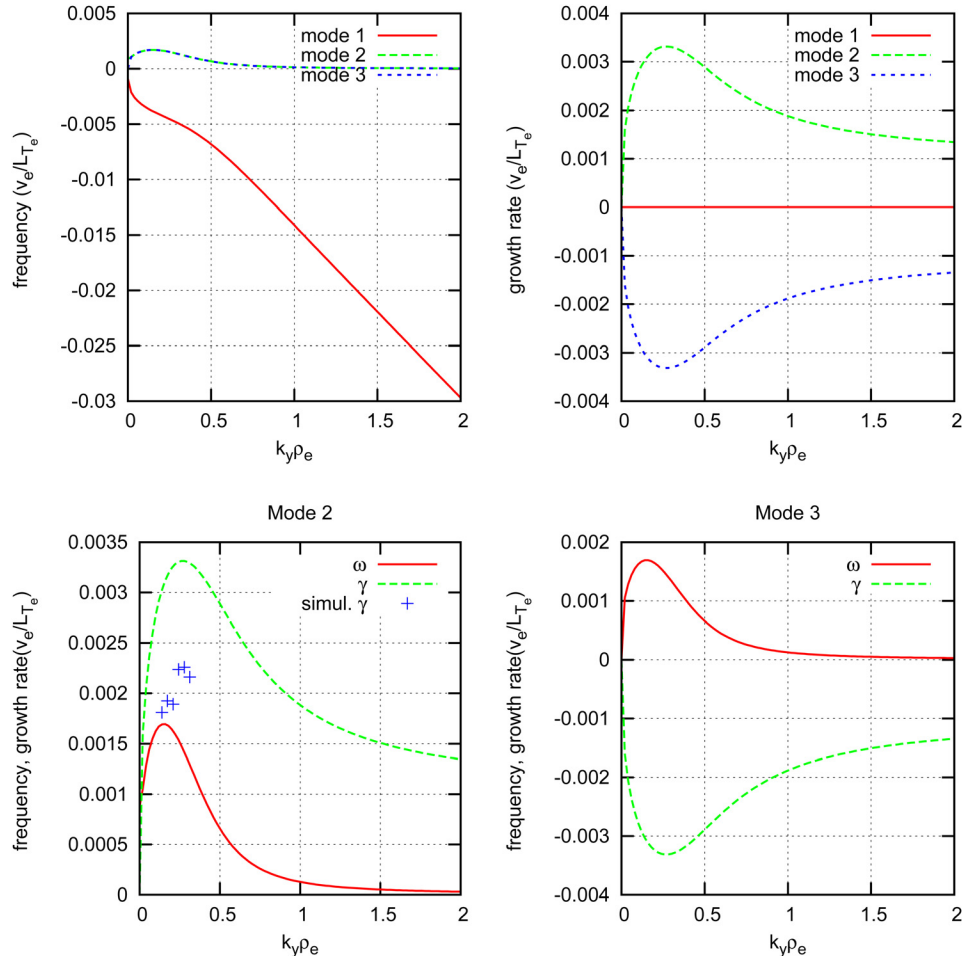


FIG. 3. (Color online) The dispersion relation of the slab ETG without density gradient, given by Eq. (1). These are three modes: mode 1 is purely damping; mode 2 and mode 3 are complex conjugates. We are interested in the unstable mode 2, whose growth rate is larger than the frequency. The growth rates obtained from linear simulations are shown as blue crosses.

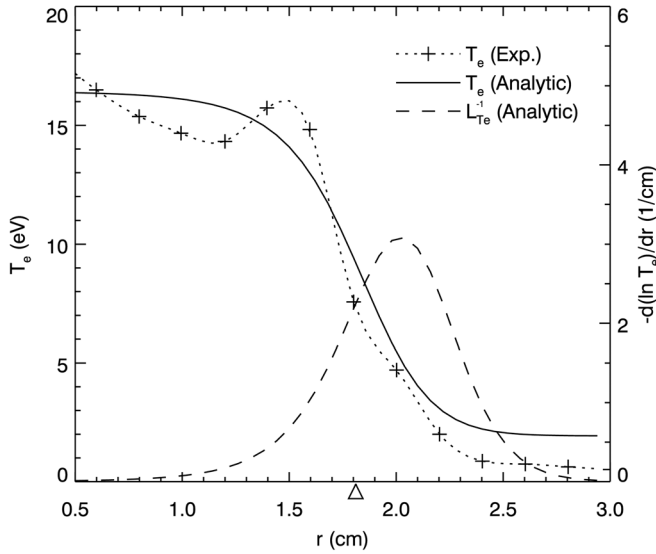


FIG. 4. The electron temperature profile for GTC simulations. The experimental results are shown as the dotted curve with plus signs. The analytic model is depicted by the solid curve, and the dash curve is its inverse scale length  $1/L_{Te}$ . The triangle marks the radial position of the maximum gradient of the model.

$$t \rightarrow tc_{s,e}/R_0, \quad l \rightarrow l/R_0, \quad (2)$$

where  $R_0 = 300$  cm and  $c_{s,e} = \sqrt{T_i/m_e} \approx 7.27 \times 10^7$  cm/s. The time step  $t_0 = 0.0025 \times c_{s,e}/R_0 \approx 10^{-8}$  s. For a typical run, we employ approximately  $150 \times 600 \times 32$  (in the radial, poloidal, and toroidal direction, respectively) cells and 1000 electrons per cell. That corresponds to a perpendicular spatial resolution of  $\sim 0.35\rho_{e0}$ . It takes about 10 h to run on NERSC Hopper or TACC Ranger with 2048 nodes for simulating 8000 time steps.

In our simulation model, electrons are advanced by electrostatic gyrokinetic equation using  $\delta f$  algorithm<sup>9</sup>

$$\frac{dw_e}{dt} = (1 - w_e) \left[ -\mathbf{v}_E \cdot \frac{\nabla f_{0e}}{f_{0e}} - (\mathbf{e}\mathbf{b} \cdot \nabla \phi) \frac{1}{m_e f_{0e}} \frac{\partial f_{0e}}{\partial v_{||}} \right], \quad (3)$$

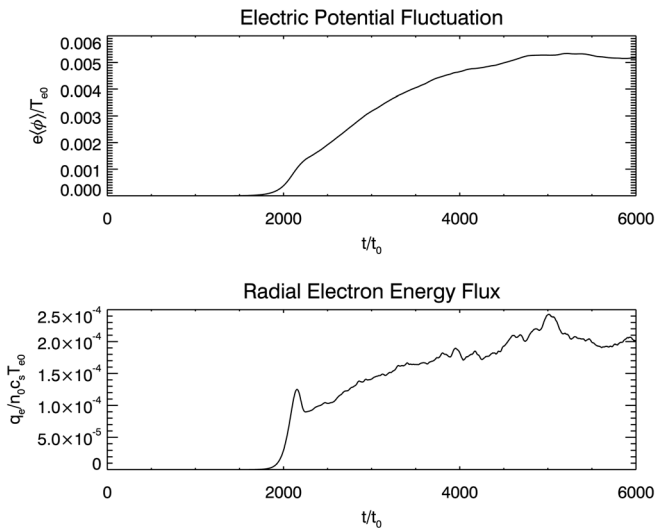


FIG. 5. The time evolution of the root-mean-square of the electric potential  $\langle\phi\rangle = \int_V \sqrt{\phi^2} d^3r / \int_V d^3r$ , and the radial electron energy flux  $q_e = \int \int \frac{eE_0}{2B} m_e (v^2 - v_{||}^2) \delta f d^3v d^3r / \int_V d^3r$ .

where  $w_e \equiv \delta f_e/f_{0e}$  and  $f_{0e}$  is the background electron distribution function. Ions are treated as adiabatic

$$\frac{\delta f_i}{f_i} = -\frac{e\phi}{T_i}, \quad (4)$$

which is valid when  $k_{\perp}\rho_i \gg 1$ . The boundary condition in  $z$  direction (along  $\mathbf{B}$  field) is periodic, and the electric potential  $\phi$  vanishes at the inner ( $r/a = 0.2$ ) and outer ( $r/a = 0.8$ ) radii.

### 1. Modeling electron temperature and density profiles

As shown in Fig. 4, the background temperature profile used in the simulations are modeled by the analytic formula

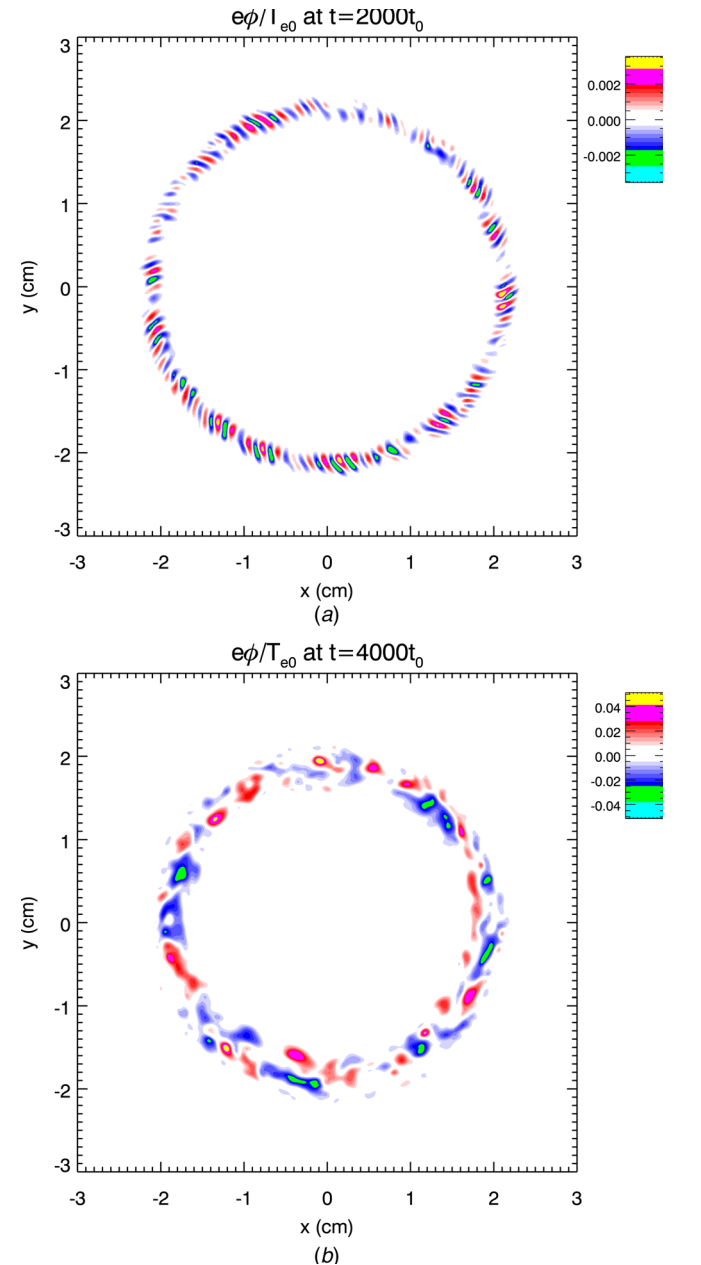


FIG. 6. (Color online) Contours of the electric-potential fluctuation in the poloidal plane at (a) linear stage  $t = 2000t_0$  and (b) nonlinear stage  $t = 4000t_0$ . In the linear stage, the fastest growing mode with  $m \approx 70$  and  $n = 2$  ( $m$  and  $n$  are the poloidal and the parallel mode number, respectively) dominates, while in the nonlinear stage,  $m \approx 12$  and  $n = 1$  mode dominates.

## Electric Potential Fluctuation Spectra

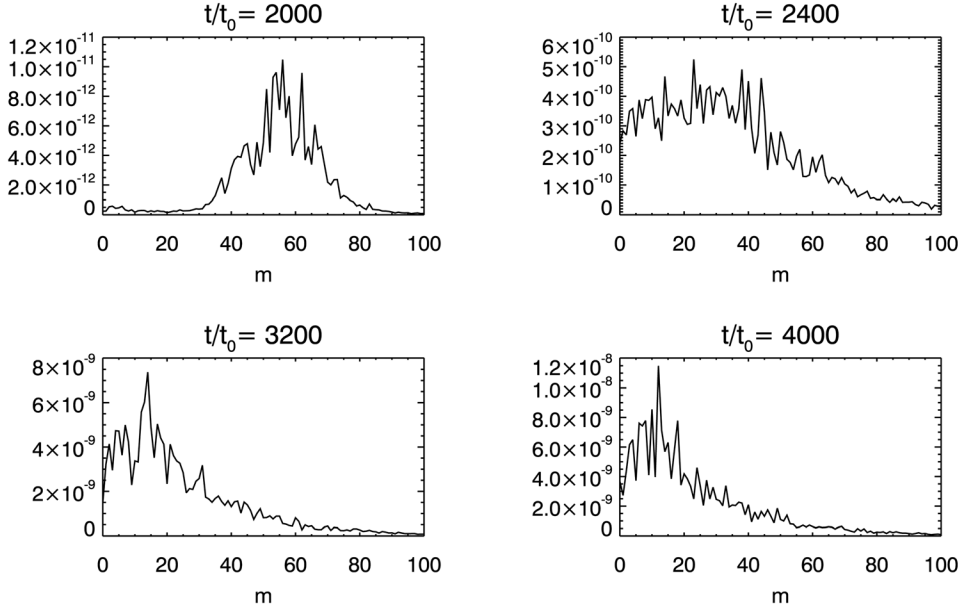


FIG. 7. The poloidal power spectra of the electric potential fluctuation at  $r = 1.88$  cm. The strong nonlinear coupling causes inverse cascading, and the peaking mode shifts from  $m = 55$  down to  $m = 12$ .

$$T_e = T_{e0} \left[ 1 + c_1 \left( \tanh \frac{c_2 - r^2/a^2}{c_3} - 1 \right) \right] \quad (5)$$

with  $[c_1, c_2, c_3] = [0.44, 0.36, 0.14]$ . This background profile is fixed during the simulation. For the density, we use a flat profile, i.e.,  $n_e(r) = \text{const}$ . The maximum temperature gradient is located at  $r = 1.8$  cm, but  $L_{T_e}^{-1}$  peaks at  $r = 2.1$  cm with maximum  $L_{T_e} \approx 0.3$  cm, where the linear growth rate is largest. The drift frequency at this peak is

$$\omega_{*T_e} = k_y \rho_e v_{te} / L_{T_e} = m \times 2\pi \times 0.193 \text{ MHz}. \quad (6)$$

## 2. Time history

Fig. 5 shows the time history of the averaged electric potential fluctuation and electron energy flux. It is clear that

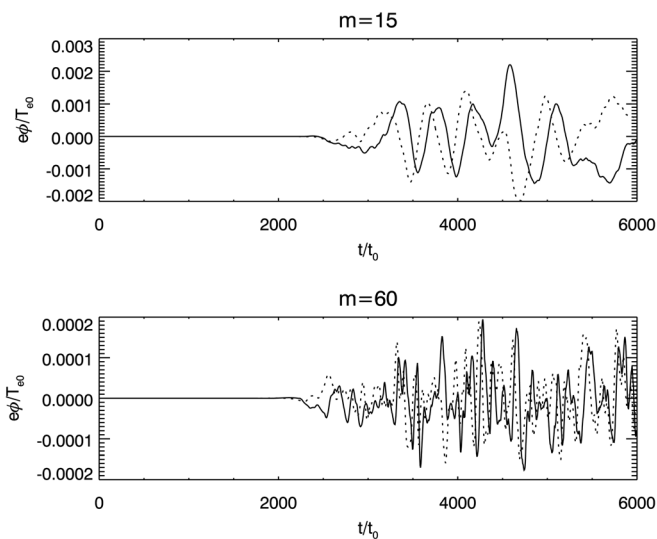


FIG. 8. The time history of the electric potential of  $m = 15$  mode and  $m = 60$  mode. The solid line is the real part and the dotted line is the imaginary part. The frequency of  $m = 15$  mode is about 0.24 MHz in the nonlinear stage.

during  $0 < t < 2200t_0$ , both quantities grow exponentially, corresponding to a linear stage. The growth rates for a few modes obtained from the simulations are shown in Fig. 3 as blue crosses. Thereafter, ETG modes saturate and when  $t > 4000t_0$ , it enters a quasi-steady state.

Two contours of the electric potential at  $t = 2000t_0$  and  $t = 4000t_0$  are shown in Fig. 6 representing a typical linear and nonlinear case, respectively. The strong nonlinear effect causes inverse cascading, with energy transfer from short poloidal wave length (large  $m$  number) modes to long wave length modes (small  $m$  number). The power spectra of signals measured at  $r = 1.88$  cm for  $t = 2000t_0$ ,  $t = 2400t_0$ ,  $t = 3200t_0$ , and  $t = 4000t_0$  are shown in Fig. 7.

## 3. Mode history

The mode history of  $m = 15$  and  $m = 60$  are shown in Fig. 8.  $m = 60$  is the fastest growing mode at late linear stage and  $m = 15$  is the dominant mode in the nonlinear stage. The frequency of  $m = 15$  mode in the plasma frame is about 0.24 MHz, close to the experimental measurements (0.3–0.5 MHz).

## 4. Radial profile of the electric potential fluctuations

The radial profile of root-mean-square values of the potential fluctuations  $\phi_{\text{rms}}(r)$  at different stages ( $t = 2000t_0$ ,  $3000t_0$ , and  $4000t_0$ ) are shown in Fig. 9. The fluctuation  $e\phi/T_{e0}$  can go as high as 2%, and the peak of the fluctuation moves radially inward. This value is lower than the experimental results of  $e\phi/T_e \sim 5\%$ . There are also small outward extending vortex structures or “fingers” in this nonlinear state. Both of them may be caused by the density fluctuation. In this paper, we used  $\delta f$  algorithm and fix the background temperature profile while letting the density fluctuation evolve freely and in the nonlinear stage, the density profile is no longer flat but has gradients away from the maximum

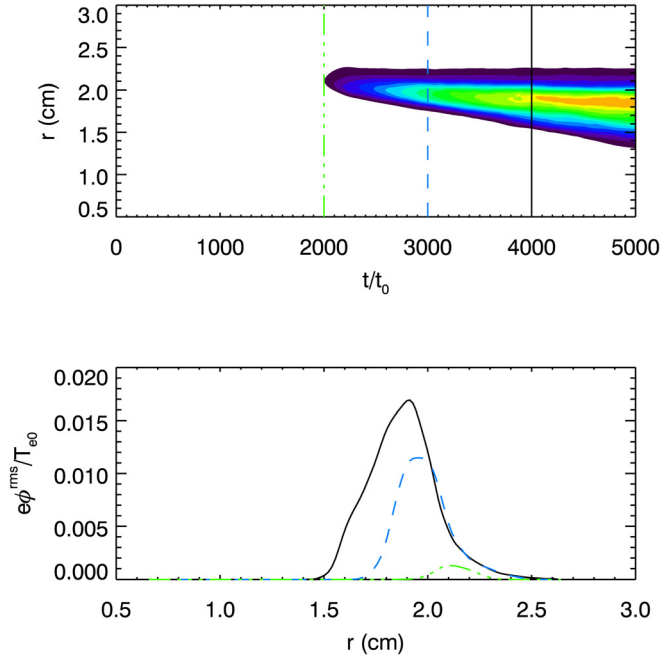


FIG. 9. (Color online) The evolution of the radial profile of the electric potential fluctuation averaged over  $r = \text{constant}$  surface, with green dash-dot-dot curve for  $t = 2000t_0$ , blue dash curve for  $t = 3000t_0$ , and black solid curve for  $t = 4000t_0$ . The background electron temperature profile is fixed with the maximum gradient at  $r = 1.8$  cm and maximum  $1/L_{Te}$  at  $r = 2.1$  cm. Due to nonlinear effects, the peak of the fluctuation profile moves inward.

temperature gradient. These trigger  $\eta_e$ -mode causing fluctuations to spread inward and outward.

### 5. Heat flux

The evolution of the radial profile of electron energy flux given by the correlation function of  $\langle v_r \delta T_e \rangle$  is shown in Fig. 10. The nonlinear thermal flux extends over a broad radial region. The electron thermal conductivity can be estimated by

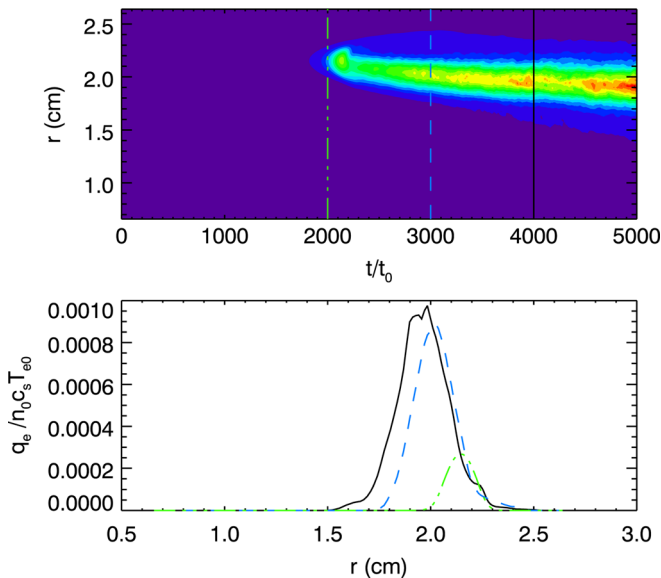


FIG. 10. (Color online) The evolution of the radial profile of the electron energy flux, with green dash-dot-dot curve for  $t = 2000t_0$ , blue dash curve for  $t = 3000t_0$ , and black solid curve for  $t = 4000t_0$ .

$$\chi_e = -q_e/n_e \nabla T_e. \quad (7)$$

At  $t = 4000t_0$  and  $r = 1.9$  cm,  $\chi_e/D_{gB} \approx 0.43$ , where  $D_{gB} = \frac{\rho_e c T_e}{a e B}$ .

## B. Parametric variations of measured signal and those from simulations

### 1. Variation of fluctuations with the temperature gradient

In order to study the dependence of electron heat flux on the temperature gradient, we compare three cases with the maximum  $L_{Te} = 0.33$  cm,  $L_{Te} = 0.45$  cm, and  $L_{Te} = 0.66$  cm. The profiles are shown in Fig. 11(a), and the comparison of the maximum potential fluctuation, the maximum electron

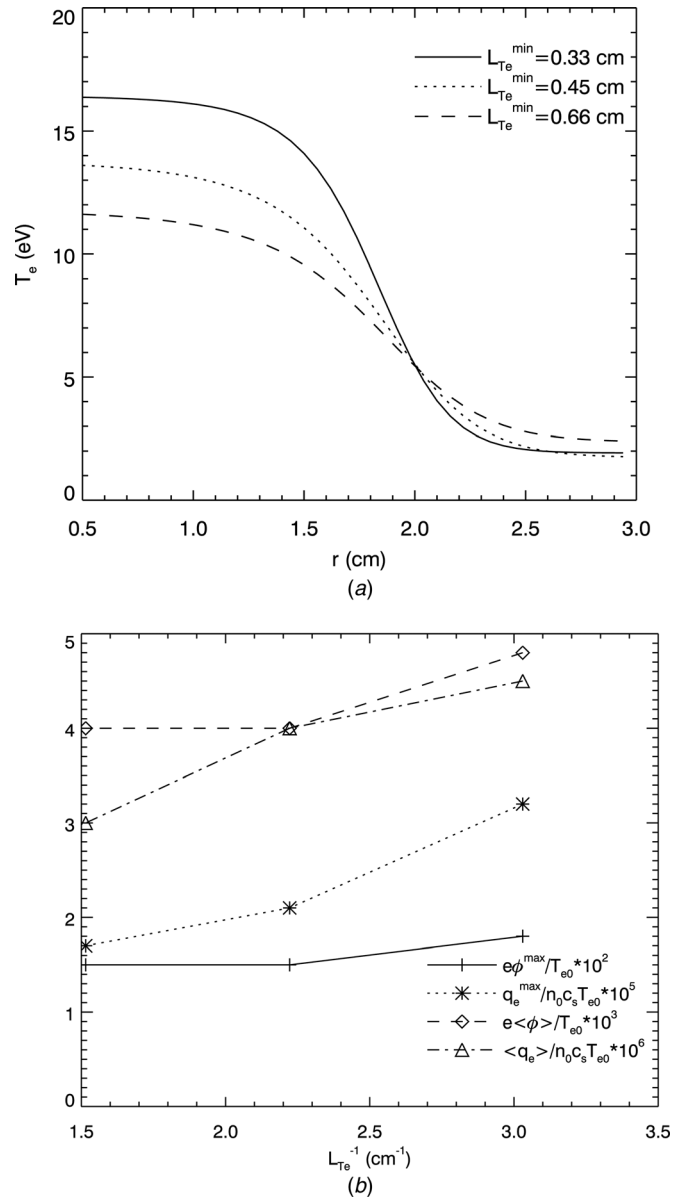


FIG. 11. (a) Various background electron temperature profiles for simulations, with the minimum  $L_{Te} = 0.33$  cm, 0.45 cm, and 0.66 cm. (b) Comparison of the maximum potential fluctuation, the maximum electron heat flux, the averaged potential fluctuation, and the averaged electron heat flux between these simulations.

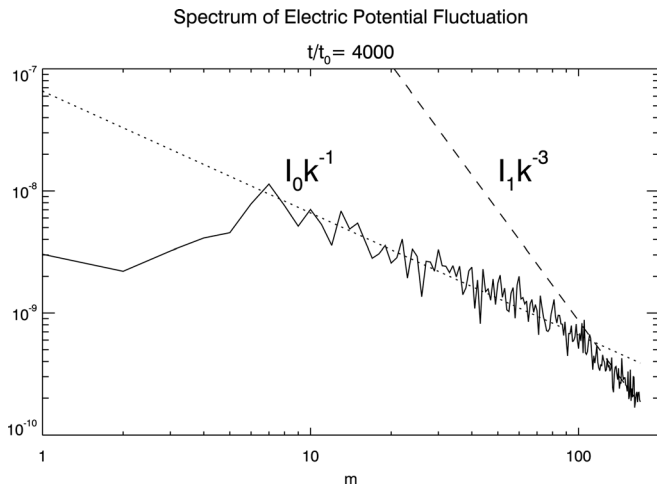


FIG. 12. The power spectrum of electric potential fluctuation in the nonlinear stage. It shows a power-law decay with the intensity proportional to  $k^{-1}$  for  $10 < m < 100$  modes and  $k^{-3}$  for  $m > 100$  modes.

heat flux, the averaged potential fluctuation, and the averaged electron heat flux is shown in Fig. 11(b). The turbulence amplitude changes slower than the thermal flux, which indicates the turbulent transport may rely more on the correlation length and the temperature-fluctuation-to-potential phase than the turbulence intensity.

## 2. Variation of the fluctuations with parallel wavenumber or axial length

We also study the dependence of ETG modes on the parallel wavenumber by changing the major radius (or equivalently the machine length) from  $R_0 = 300$  cm to  $R_0 = 100$  cm. The case with  $R_0 = 100$  cm shows very similar features as  $R_0 = 300$  cm except that in the linear stage, the fastest growing mode has  $n = 1$  rather than  $n = 2$  and the final quasi-steady-state is dominated by  $m = 15$  mode (cf.  $m = 12$  in Fig. 6).

## C. Nonlinear saturation of ETG modes

As shown in Sec. IV B 2, the inverse cascading of ETG energy from high- $m$  mode to low- $m$  mode indicates strong nonlinear coupling. The nonlinear theory for the saturation of toroidal ETG/ITG modes can be found in Refs. 7 and 14. A nonlinear saturation mechanism for slab ITG can be found in Refs. 15 and 16. In order to study the power spectrum, a higher spatial resolution simulation with  $200 \times 1000 \times 32$  grids and  $t_0 = 0.005 \times c_{s,e}/R_0$  is carried out. The log-log plot of the nonlinear power spectrum of the electric potential  $\phi$  fluctuations in Fig. 12 shows a power law decay with  $|\phi_m|^2$  proportional to  $m^{-p}$ , with  $p = 1$  for  $10 < m < 100$  and  $p = 3$  for  $m > 100$ . This double-power-law spectrum agrees with the prediction by the renormalization theory in Ref. 14, which involved a three-wave interaction and non-resonant mode coupling under the quasi-normal approximation for the fourth order correlation function. The argument is based on the fact that the energy  $\langle v_E^2 \rangle$  should be finite, which leads to a decay rate of  $I(k)$  faster than  $k^{-3}$  for high  $k$  modes. The turning point in present work ( $m \sim 100$ ) is, however, higher than that in Ref. 14 ( $m \sim 60$ ) due to the absence of toroidal effects.

## V. CONCLUSIONS

The variable electron temperature gradient driven high frequency drift wave turbulence produced in the CLM experiment is well interpreted by the GTC gyrokinetic code. In the terminology of simulation modeling, the agreement allows one to state the GTC code is verified by the data from the CLM experiment. The amplitude of saturation level is set principally by the nonlinear cascade from the fastest linearly growing modes with  $m \sim 70$  as given by the linear kinetic dispersion relation to the nonlinear spectrum peaked at  $m \sim 15$ . These results can be explained by the early nonlinear model of the inverse cascade given in Horton *et al.*<sup>7</sup> Thus, the verification of the strong inverse cascade in the CLM data using the GTC gyrokinetic equation simulations is an important confirmation of early turbulence theory models for drift wave systems.

Future work is planned to extend the simulations to the low- $m$  mode numbers  $m < 10$  where the plasma response functions are of the usual ion drift waves and acoustic modes. This involves coupling the simulations to the conventional ion scale simulations and theories and it may further lower the rms amplitude of the high- $m$  modes in the spectrum.

## ACKNOWLEDGMENTS

The authors would like to thank Professor Sadri Benkadda for useful discussions at the University de Provence where part of this work was carried out. The work was supported under the U.S. Department of Energy grants to Institute for Fusion Studies, University of Texas at Austin and the University of California at Irvine and a grant from the OFE, U.S. Department of Energy for support at Columbia University.

- <sup>1</sup>W. Horton, H. V. Wong, P. J. Morrison, A. Wurm, J. H. Kim, J. C. Perez, J. Pratt, G. T. Hoang, B. P. LeBlanc, and R. Ball, *Nucl. Fusion* **45**(8), 976 (2005).
- <sup>2</sup>S. M. Kaye, F. M. Levinton, D. Stutman, K. Tritz, H. Yuh, M. G. Bell, R. E. Bell, C. W. Domier, D. Gates, W. Horton, J. Kim, B. P. LeBlanc, N. C. Luhmann, Jr., R. Maingi, E. Mazzucato, J. E. Menard, D. Mikkelsen, D. Mueller, H. Park, G. Rewoldt, S. A. Sabbagh, D. R. Smith, and W. Wang, *Nucl. Fusion* **47**, 499 (2007).
- <sup>3</sup>G. T. Hoang, C. Bourdelle, X. Garbet, B. Pégourié, J. F. Artaud, V. Basiuk, J. Bucalossi, C. F. Bonizet, F. Claret, L.-G. Eriksson, C. Gil, R. Guirlet, F. Imbeaux, J. Lasalle, C. Lowry, B. Schunke, J. L. Séguin, J. M. Travère, E. Tsitrone, and L. Vermare, *Nucl. Fusion* **46**, 306 (2006).
- <sup>4</sup>E. Asp, J.-H. Kim, W. Horton, L. Porte, S. Alberti, A. Karpushov, Y. Martin, O. Sauter, G. Turri, and Tcv Team, *Phys. Plasmas* **15**(8), 082317 (2008).
- <sup>5</sup>E. Mazzucato, D. R. Smith, R. E. Bell, S. M. Kaye, J. C. Hosea, B. P. Leblanc, J. R. Wilson, P. M. Ryan, C. W. Domier, N. C. Luhmann, Jr., H. Yuh, W. Lee, and H. Park, *Phys. Rev. Lett.* **101**(7), 075001 (2008).
- <sup>6</sup>X. Wei, V. Sokolov, and A. K. Sen, *Phys. Plasmas* **17**(4), 042108 (2010).
- <sup>7</sup>W. Horton, B. G. Hong, and W. M. Tang, *Phys. Fluids* **31**, 2971 (1988).
- <sup>8</sup>Y. C. Lee, J. Q. Dong, P. N. Guzdar, and C. S. Liu, *Phys. Fluids* **30**, 1331 (1987).
- <sup>9</sup>I. Holod, W. L. Zhang, Y. Xiao, and Z. Lin, *Phys. Plasmas* **16**(12), 122307 (2009).
- <sup>10</sup>Z. Lin, *Science* **281**(5384), 1835 (1998).
- <sup>11</sup>Y. Xiao and Z. Lin, *Phys. Rev. Lett.* **103**(8), 085004 (2009).
- <sup>12</sup>Z. Lin, L. Chen, and F. Zonca, *Phys. Plasmas* **12**(5), 056125 (2005).
- <sup>13</sup>W. Deng, Z. Lin, I. Holod, X. Wang, Y. Xiao, and W. Zhang, *Phys. Plasmas* **17**(11), 112504 (2010).
- <sup>14</sup>W. Horton, Jr., D. I. Choi, and W. M. Tang, *Phys. Fluids* **24**(6), 1077 (1981).
- <sup>15</sup>S. E. Parker and A. K. Sen, *Phys. Plasmas* **9**, 3440 (2002).
- <sup>16</sup>V. Sokolov and A. K. Sen, *Nucl. Fusion* **45**, 439 (2005).